This is an open access article published under an ACS AuthorChoice License, which permits copying and redistribution of the article or any adaptations for non-commercial purposes.

ACS OMEGA

Article

Cite This: ACS Omega 2018, 3, 16328−16337

http://pubs.acs.org/journal/acsodf

# $Zn^{2+}$ Ion Surface Enrichment in Doped Iron Oxide Nanoparticles Leads to Charge Carrier Density Enhancement

Stanley Bram,[†,#] Matthew N. Gordon,[†] Michael A. Carbonell,[†] Maren Pink,[†] Barry D. Stein,[‡] David Gene Morgan,[†] David Aguilà,[§] Guillem Aromí,[§] Sara E. Skrabalak,[†] Yaroslav Losovyj,*[,†] and Lyudmila M. Bronstein*[,†,∥,⊥]

[†]Department of Chemistry, Indiana University, 800 E. Kirkwood Avenue, Bloomington, Indiana 47405, United States

[‡]Department of Biology, Indiana University, 1001 E. Third Street, Bloomington, Indiana 47405, United States

[§]Departament de Química Inorgànica i Orgànica and IN2UB, Universitat de Barcelona, Diagonal 645, Barcelona 08028, Spain

[∥]A.N. Nesmeyanov Institute of Organoelement Compounds, Russian Academy of Sciences, 28 Vavilov Street, Moscow 119991, Russia

[⊥]Department of Physics, Faculty of Science, King Abdulaziz University, P.O. Box 80303, Jeddah 21589, Saudi Arabia

Supporting Information

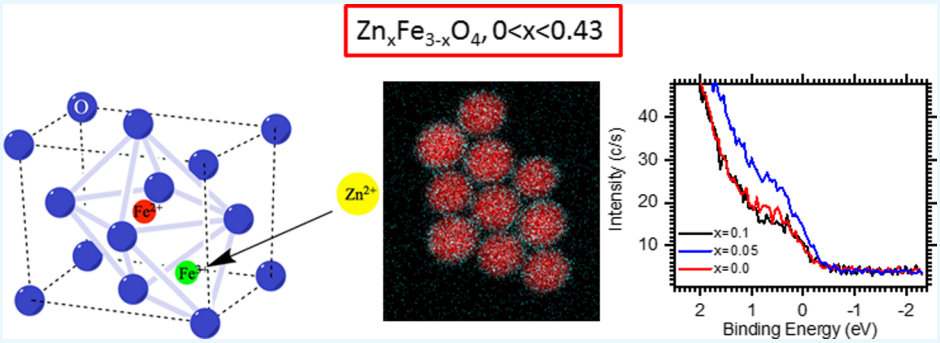


**ABSTRACT:** Here, we report the development of monodisperse Zn-doped iron oxide nanoparticles (NPs) with different amounts of Zn ($Zn_xFe_{3-x}O_4$, $0 < x < 0.43$) by thermal decomposition of a mixture of zinc and iron oleates. The as-synthesized NPs show a considerable fraction of wüstite (FeO) which is transformed to spinel upon 2 h oxidation of the NP reaction solutions. At any Zn doping amounts, we observed the enrichment of the NP surface with $Zn^{2+}$ ions, which is enhanced at higher Zn loadings. Such a distribution of $Zn^{2+}$ ions is attributed to the different thermal decomposition profiles of Zn and Fe oleates, with Fe oleate decomposing at much lower temperature than that of Zn oleate. The decomposition of Zn oleate is, in turn, catalyzed by a forming iron oxide phase. The magnetic properties were found to be strongly dependent on the Zn doping amounts, showing the saturation magnetization to decrease by 9 and 20% for $x = 0.05$ and 0.1, respectively. On the other hand, X-ray photoelectron spectroscopy near the Fermi level demonstrates that the $Zn_{0.05}Fe_{2.95}O_4$ sample displays a more metallic character (a higher charge carrier density) than undoped iron oxide NPs, supporting its use as a spintronic material.

## INTRODUCTION

Magnetic nanoparticles (NPs), in particular doped or undoped superparamagnetic iron oxide NPs (IONPs), receive considerable attention because of exciting biomedical applications. IONPs are commonly recommended for medical applications because they are easily metabolized or degraded in vivo[1,2] and FDA-approved,[3] opening up numerous possibilities for their utilization in magnetic resonance imaging (MRI), magnetic particle imaging, hyperthermia, magnetically controlled drug delivery, and so forth.[4−19] In all of these cases, the higher the magnetic moment/saturation magnetization of the material, the stronger the magnetic response and its effects on related properties. One of the ways to increase the saturation magnetization is to increase the IONP size, while keeping it below the size at which the blocking temperature ($T_B$) exceeds room temperature. $T_B$ is the temperature below which hysteresis can be observed. This is the consequence of magnetite or maghemite NPs displaying ferrimagnetic properties,[20] making NPs prone to aggregation. This critical size is strongly dependent on the shape and arrangement of the NPs.[19−24]

Because the magnetic properties of IONPs are size-dependent, particle monodispersity is of crucial importance. Monodisperse IONPs are commonly prepared by thermal decomposition of iron acetylacetonates[25−27] or carboxylates[27−31] in high-boiling solvents in the presence of fatty

Received: September 17, 2018
Accepted: November 19, 2018
Published: November 30, 2018


© 2018 American Chemical Society

DOI: 10.1021/acsomega.8b02411
ACS Omega 2018, 3, 16328−16337

Table 1. Synthesis Conditions for Zn-Doped Iron Oxide Samples, $Zn_xFe_{3-x}O_4$, at Various Doping Concentrations

| sample notation | "$x$" value in $Zn_xFe_{3-x}O_4$[a] | FeOl, g | ZnOl, g | eicosane, g | oleic acid, mL | NP diameter of oxidized NPs, nm |
|---|---|---|---|---|---|---|
| IONPs | 0 | 1.66 | 0.00 | 6.48 | 1.69 | 16.6 ± 0.9 |
| $Zn_{0.05}Fe_{2.95}O_4$ | 0.05 | 1.305 | 0.015 | 5.154 | 1.03 | 17.2 ± 0.8 |
| $Zn_{0.1}Fe_{2.9}O_4$ | 0.1 | 1.498 | 0.035 | 5.987 | 1.20 | 17.1 ± 1.0 |
| $Zn_{0.19}Fe_{2.81}O_4$ | 0.19 | 1.613 | 0.075 | 6.593 | 1.32 | 17.2 ± 0.7 |
| $Zn_{0.35}Fe_{2.65}O_4$ | 0.35 | 1.240 | 0.12 | 5.310 | 1.00 | 17.3 ± 0.9 |
| $Zn_{0.43}Fe_{2.57}O_4$ | 0.43 | 1.371 | 0.159 | 5.976 | 1.20 | 19.2 ± 0.8 |

[a]By loading.

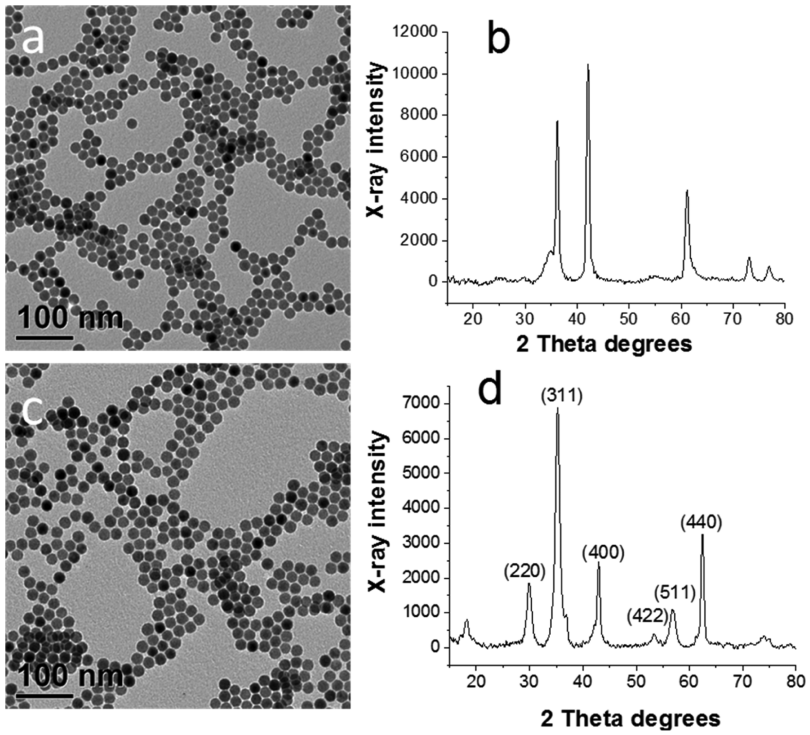


Figure 1. TEM images (a,c) and XRD patterns (b,d) of as-synthesized (a,b) and oxidized $Zn_{0.35}Fe_{2.65}O_4$ (c,d).

acids and/or oleylamine as surfactants. Comparatively large IONPs (15−30 nm) can be prepared by direct, one-pot thermal decomposition of iron oleates.[28,29,32]

Another viable approach to increase magnetization is doping of iron oxide with such metal ions as $Zn^{2+}$, $Co^{2+}$, $Mn^{2+}$, $Cu^{2+}$, and so forth.[33−36] Considering that IONPs should preserve biocompatibility for medical applications, the doped IONPs should also be benign. Recent studies indicated that Zn-doped magnetite NPs remain nearly nontoxic,[37,38] while for other doped IONPs, toxicology studies are scarce. The majority of Zn-doped IONPs is synthesized by thermal decomposition of iron and zinc acetylacetonates,[6] $Fe(acac)_3$ and $ZnCl_2$,[6,34] by a cationic exchange with $Zn^{2+}$ ions in IONPs,[33] or by co-precipitation of corresponding metal salts.[34] This allows formation of Zn-doped IONPs in the size range 8−19 nm. Maiti et al. reported formation of Zn ferrite NPs by thermal decomposition of Zn and Fe oleates, but the resultant NPs were polydisperse in size and shape.[39]

In addition to biomedical applications, magnetite and doped IONPs and thin films hold promise as spintronic materials with tunable electrical and magnetic properties.[40−45] This is due to the fact that these oxides demonstrate half metal properties.[46] While for biomedical applications of magnetic NPs, the whole focus is on enhanced magnetization, for spintronics, a balance of electrical conduction and magnetism is needed which, in turn, is determined by the density and hopping amplitude of the itinerant charge carriers in the octahedral sites of the spinel structure.[41]

In this work, we studied the formation, structure, and properties of monodisperse Zn-doped IONPs of different compositions, whose sizes are in the range of 16−25 nm depending on the reaction temperature (determined by solvent choice) and whose magnetization strongly depends on the amount of the doping metal. We demonstrate that the distribution of $Zn^{2+}$ ions in the spinel structure of NPs determines both their magnetic and charge carrier properties. At the lowest Zn loading, the moderate accumulation of $Zn^{2+}$ ions on the IONP surface increases the metallic character of these NPs while the saturation magnetization is largely preserved, making them promising as spintronic materials.

## RESULTS AND DISCUSSION

**Synthesis of Zn-Doped IONPs and Their Oxidation.** Zn-doped IONPs have been synthesized by thermal decomposition of a mixture of iron (FeOl) and zinc (ZnOl) oleates at a boiling temperature of a saturated hydrocarbon (eicosane or docosane). The transmission electron microscopy (TEM) image of the as-synthesized sample prepared at $x = 0.35$ (Table



DOI: 10.1021/acsomega.8b02411
ACS Omega 2018, 3, 16328−16337

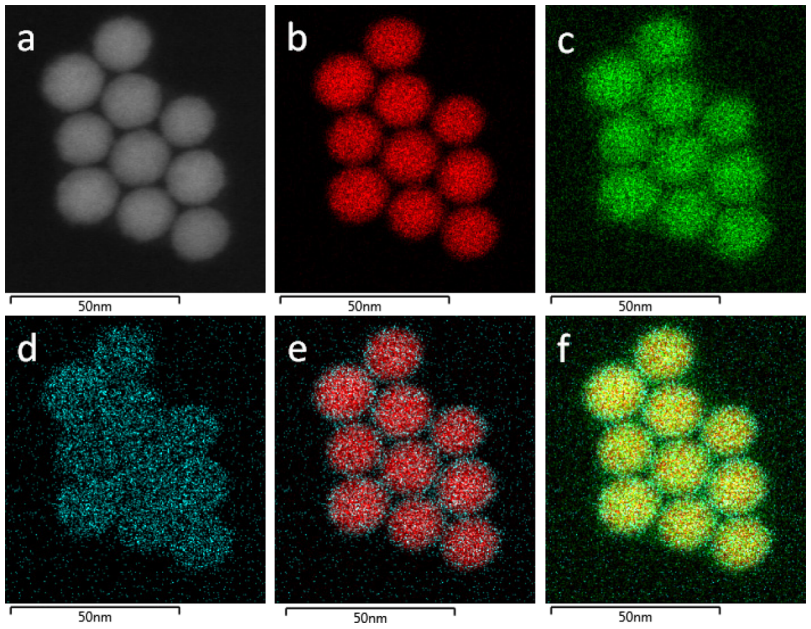


**Figure 2.** STEM dark-field image (a) and STEM EDS maps of Fe (b), O (c), Zn (d), the Fe−Zn mix (e), and the Fe−Zn−O mix (f) of $Zn_{0.35}Fe_{2.65}O_4$.

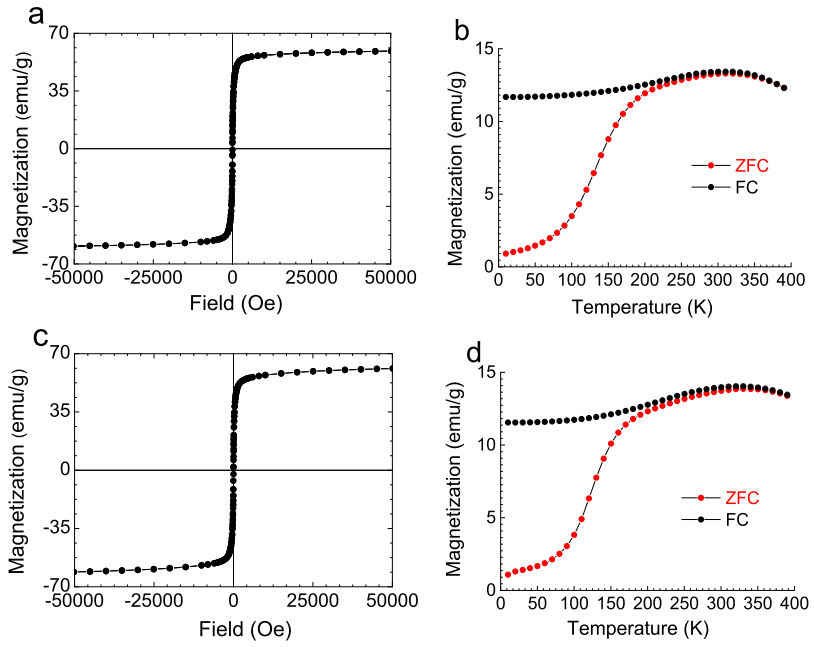


**Figure 3.** Isothermal magnetization curves at 300 K (a,c) and ZFC−FC susceptibility curves (b,d) of IONPs (a,b) and $Zn_{0.05}Fe_{2.95}O_4$ (c,d).

1) shows spherical monodisperse NPs with a mean diameter of 17.1 nm (Figure 1a). The X-ray powder diffraction (XRD) pattern of the same sample (Figure 1b) reveals that the NPs consist of mainly wüstite (FeO) with a small fraction of magnetite ($Fe_3O_4$), similar to undoped NPs prepared solely from iron oleate.[32] It was demonstrated that FeO or FeO/$Fe_3O_4$ NPs can be successfully oxidized to $Fe_3O_4$ or a mixture of $Fe_3O_4$ and $\gamma$-$Fe_2O_3$ by simple heating of the reaction solution at 200 °C for 2 h.[47,48] This results in a minor increase of the diameter (to 17.3 nm, Table 1) of the monodisperse NPs (standard deviation of ∼5%) (Figure 1c) and the formation of the cubic spinel structure (JCPDS 77-1545) as can be seen from the XRD pattern of the oxidized sample (Figure 1d). The crystallite size determined using the Scherrer equation is 14.3 nm, indicating that the NPs are not single crystals. When eicosane was replaced with docosane (set reaction temperature was 380 °C), the NP size increased to 25.5 nm with a NP size distribution of 5.4% (Figure S1, the Supporting Information). For the sake of comparison, we synthesized all other samples in eicosane at otherwise identical conditions to obtain similar particle sizes (Table 1). In the following sections, only oxidized Zn-doped IONPs will be discussed.

**Structure of Zn-Doped IONPs.** The absence of an additional ZnO phase for Zn-doped IONPs suggests that the $Zn^{2+}$ ions are incorporated in the spinel phase. A closer look at the (311) reflection in the XRD patterns of undoped and Zn-doped IONPs with $x$ = 0.1 and 0.19 (Table 1) shows that it is



DOI: 10.1021/acsomega.8b02411
ACS Omega 2018, 3, 16328−16337

Table 2. Data of Magnetic Measurements and X-ray Photoelectron Spectroscopy (XPS) for Zn-Doped IONPs, $Zn_xFe_{3-x}O_4$, at Various Doping Concentrations

| sample notation | "$x$" value in $Zn_xFe_{3-x}O_4$[a] | NP diameter, nm | $M_s$, emu/g[b] | $T_B$ | $M_s^n$ emu/g[c] | Fe 2p, at. % | Zn 2p, at. % | Fe 3p, at. % | Zn 3p, at. % |
|---|---|---|---|---|---|---|---|---|---|
| IONPs | 0 | 16.6 | 56.7 | 270 | 60.5 | 100 | 0 | 100 | 0 |
| $Zn_{0.05}Fe_{2.95}O_4$ | 0.05 | 17.2 | 57.2 | 270 | 55.2 | 96.6 | 4.7 | 99 | 1.0 |
| $Zn_{0.1}Fe_{2.9}O_4$ | 0.1 | 17.1 | 49.2 | 200 | 48.9 | 84.7 | 11.5 | 97.4 | 2.6 |
| $Zn_{0.19}Fe_{2.81}O_4$ | 0.19 | 17.2 | 25.9 | 220 | 25.7 | 80 | 20 | 93.1 | 6.9 |
| $Zn_{0.35}Fe_{2.65}O_4$ | 0.35 | 17.3 | 25.9 | 210 | 25.7 | 74.8 | 25.2 | 90.7 | 9.3 |
| $Zn_{0.43}Fe_{2.57}O_4$ | 0.43 | 19.2 | | | | 72.8 | 27.2 | 86.9 | 13.1 |

[a]By loading. [b]Saturation magnetization at 300 K at the magnetic field strength of 10 kOe. [c]Normalized saturation magnetization adjusted for 17 nm NPs.

slightly shifted to smaller angles (Figure S2, Supporting Information), which could be attributed to the substitution of $Fe^{3+}$ (ionic radius of 0.49 nm) ions in tetrahedral sites of the IONP spinel structure by $Zn^{2+}$ (ionic radius of 0.74 nm).[49] The high-resolution TEM (HRTEM) image presented in Figure S3 Supporting Information shows that the NPs are highly crystalline although they are not single crystals, which is in agreement with the XRD data.

Figure 2 displays the scanning TEM (STEM) dark-field image and energy dispersive spectroscopy (EDS) maps of $Zn_{0.35}Fe_{2.65}O_4$ (Table 1). The maps show that Zn, Fe, and O are present in the Zn-doped IONPs and Zn exhibits a higher abundance in the NP exterior.

**Magnetic Properties.** Magnetic measurements were performed to evaluate the magnetic behavior of these Zn-doped IONPs. Figure 3 shows the isothermal magnetization curves at 300 K and zero-field cooling (ZFC) and FC magnetization curves for undoped IONPs and $Zn_{0.05}Fe_{2.95}O_4$ NPs. ZFC−FC curves permit obtaining the blocking temperature, $T_B$, the point where the two curves merge.[50] For both samples, $T_B$ is about 270 K (Table 2), which is representative of superparamagnetic IONPs of a similar size.[51] This agrees well with the zero coercive field at 300 K, compared to the value of a several hundred Oe observed at 5 K, as is shown by zoomed in isothermal magnetization curves at 5 and 300 K (Figure S4, Supporting Information).

The data presented in Table 2 reveal that with the increase of the Zn loading first the saturation magnetization slightly increases at $x = 0.05$ and then significantly decreases when $x > 0.1$. However, a closer look at the Table 2 data reveals that the NP sizes are slightly different. To account for the differences in the NP sizes, we normalized saturation magnetization values by obtaining a magnetization per nm of the NP diameter and then multiplying this value by 17 to obtain a size normalized value for 17 nm NPs. These data show that even at $x = 0.05$, the saturation magnetization drops compared to that of undoped IONPs.

Szczerba et al. reported an increase in the saturation magnetization upon Zn doping up to $x = 0.5$; however, the NP synthesis (co-precipitation) resulted in polydisperse, partially aggregated NPs, creating too many variables for unambiguous conclusions.[34] Jang et al. observed an increase of the saturation magnetization up to $x = 0.4$, and a further decrease for $x = 0.8$, explaining it by the dominant antiferromagnetic coupling between $Fe^{3+}$ ions at the higher $Zn^{2+}$ doping.[52] At low Zn doping amounts, two $Fe^{3+}$ ions may be located in the octahedral sites (B sublattice) of spinel $ZnFe_2O_4$, while $Zn^{2+}$ ions could occupy the tetrahedral sites (A sublattice), thus preventing antiferromagnetic coupling between two $Fe^{3+}$ ions.[49] However, for higher $Zn^{2+}$ contents, $Zn^{2+}$ ions occupy the octahedral sites and then the magnetization of the samples decreases. In the other work on Zn-doped IONP clusters, the magnetization enhancement was only noticed for $x = 0.1$ and $x = 0.2$, while for $x = 0.3$, the saturation magnetization was nearly the same as that for undoped IONP clusters.[53] Similarly, the highest magnetization was observed at $x = 0.16$ for Zn-doped IONPs prepared via biosynthesis[54] or at $x = 0.11$ for Zn-doped maghemite NPs.[55]

On the other hand, epitaxial $Zn_xFe_{3-x}O_4$ thin films grown in pure Ar atmospheres demonstrated a decrease in saturation magnetization with increasing "$x$" even at the smallest Zn contents.[41] The authors believe that in this case, $Zn^{2+}$ ions also substitute $Fe^{3+}$ ions in tetrahedral sites, disrupting antiferromagnetic coupling in the A sublattice which was expected to increase magnetization. However, the simultaneous decrease of antiferromagnetic superexchange interactions between the $Fe^{3+}$ ions in tetrahedral and octahedral sites via oxygen ions makes the ferromagnetic double exchange weaker, competing with the antiferromagnetic superexchange interaction in the octahedral sites.[41] Considering that in our case, normalization has been performed and we decoupled the possible NP size influence from the influence of the Zn-doped IONP structure and composition, and the decrease of the saturation magnetization with increasing "$x$" is validated and can be explained by the reasoning suggested in ref 41.

**Ion Distribution by XPS.** To assess the oxidation state of metals and the distribution of metal species, XPS data for these samples have been recorded. The survey XPS spectrum of the Zn-doped iron oxide with the Zn fraction $x = 0.35$ is presented in Figure S5 Supporting Information. Similar survey spectra were obtained for the other samples studied. The survey spectra demonstrate the presence of Zn, Fe, O, and C (both from the surfactant and adventitious). No other elements were recorded, indicating purity of the sample. HR XPS of Zn 2p and Fe 2p regions are presented in Figure 4. In all samples, the HR Zn 2p XPS spectra display a peak with a binding energy (BE) of 1021.9 eV, which is representative of $Zn^{2+}$ (Figure 4b).[56] The HR Fe 2p XPS spectra are also alike and display a peak with the BE of 711.4 eV, which is characteristic of iron oxides (Figure 4a). A satellite normally observed for $Fe^{3+}$ ions at the 8−9 eV BE greater than the main peak is not showing. This satellite indicates the $Fe^{3+}$ ions in excess of the $Fe^{3+}/Fe^{2+} = 2{:}1$ ratio of magnetite.[57−59] The absence of this satellite is indicative of $Fe_3O_4$.[60] There is a weak satellite feature in the HR XPS Fe 2p of undoped IONPs (Figure S8, Supporting Information), indicating the excess of $Fe^{3+}$ species beyond the $Fe^{3+}/Fe^{2+} = 2{:}1$ ratio of magnetite.[57−59] This observation reveals the presence of maghemite on the NP surface. When $Zn^{2+}$ ions are incorporated, they apparently replace the extra $Fe^{3+}$ ions.



DOI: 10.1021/acsomega.8b02411
ACS Omega 2018, 3, 16328−16337

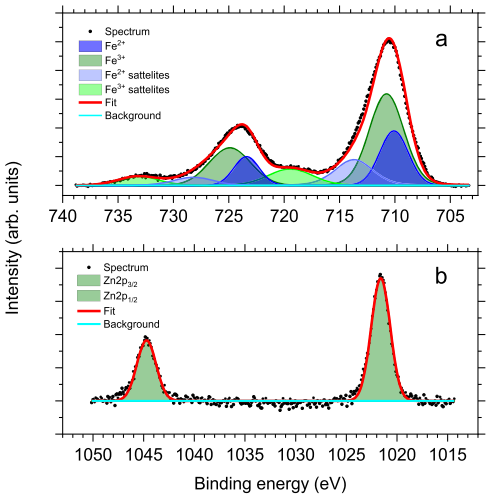


**Figure 4.** HR XPS Fe 2p (a) and Zn 2p (b) spectra of $Zn_{0.35}Fe_{2.65}O_4$.

The elemental composition of the Zn-doped IONPs has been evaluated for 2p and 3p electrons. It is well-established that the kinetic energy of 3p electrons is much greater than that of 2p electrons, allowing probing the NP surface with 2p electrons and subsurface layers with higher energy 3p electrons.[61,62] The XPS data presented in Table 2 show that the NP surface of all samples is enriched with Zn, compared to the subsurface layers. For the $Zn_{0.19}Fe_{2.81}O_4$ sample, the bulk values of the Zn and Fe contents obtained from inductively coupled plasma (ICP) are 3.6 and 52.01 wt %, respectively, producing the Fe/Zn weight ratio of 14.45. For 2p and 3p electrons (from XPS), this ratio is 3.22 and 5.34, respectively. This finding further confirms the surface enrichment with Zn. This was surprising considering that both oleates were loaded at the same time at the beginning of the reaction. It is possible that iron oleate (FeOl) decomposes at a lower temperature than zinc oleate (ZnOl), leading to the surface enrichment with Zn.

**Thermal Properties of Oleates.** To test this hypothesis, we carried out thermal gravimetric analyses (TGAs) and differential scanning calorimetry (DSC) of zinc and iron oleates at 3 °C/min (similar to the reaction conditions) as well as their mixture matching the oleate loading for $x$ = 0.35 (Figure 5). Weight loss of 5%, corresponding to the beginning of precursor decomposition, occurs at 240, 313, and 216 °C for FeOl, ZnOl, and the mixture, respectively. At ∼340 °C (the reaction temperature in eicosane), ZnOl decomposition is barely noticeable, becoming more pronounced at ∼390 °C. The DSC trace of ZnOl shows a sharp endothermic transition at 92 °C, which is assigned to melting of the hydrophobic tail ordering in ZnOl.[63] The endothermic transition assigned to the ZnOl decomposition is hardly noticeable at 390 °C.[63] It is noteworthy that the ZnOl decomposition carried out in the reaction conditions (∼340 °C) produces no ZnO NPs (see Figure S6, Supporting Information). At the same time, Zn-doped IONPs contain considerable amounts of Zn, revealing that IONPs formed early in the decomposition process catalyze the ZnOl decomposition. A similar catalyzing effect in the presence of magnetite NPs was observed for Cr acetylacetonate, whose decomposition does not occur at the reaction temperature in the absence of iron oxide.[64] Moreover, in the case of the ZnOl + FeOl mixture, the weight loss begins at the lowest temperature (Figure 5a) and the endothermic peaks assigned to the monomer formation (at about 230 °C) and its decomposition (at about 320 °C) (Figure 5b) are shifted to lower temperatures than those for iron oleate, indicating that the presence of $Zn^{2+}$ ions accelerates transformations of FeOl, while the formation of IONPs catalyzes the ZnOl decomposition, creating a gradient in the $Zn^{2+}$ ion distribution.

**Charge Carrier Transport and $Zn^{2+}$ Ion Distribution.** Table 2 data show that the normalized magnetization decreases by ∼9% for $x$ = 0.05, ∼20% for $x$ = 0.1, and then plummets by more than half starting from $x$ = 0.19. It is expected that a change (increase/decrease) of magnetization should correlate with the carrier density and subsequently with the increase of conductivity. It has been shown that thermally activated itinerant $t_{2g}$ electrons facilitate (through the hopping mechanism between $Fe^{2+}/Fe^{3+}$ ions of the B sublattice) electrical conductivity and influence the magnetic properties of $Zn_xFe_{3-x}O_4$.[41] A photoemission study of the $Zn_xFe_{3-x}O_4$ film revealed that an increase of substituted $Fe^{3+}$ ions by $Zn^{2+}$ or $Mn^{2+}$ significantly decreases the density of states (DOS) at the vicinity of the Fermi level, leading finally (at $x$ = 1) to gap opening.[65] In order to determine whether there is a correlation between the magnetic and electronic properties of the IONPs upon Zn doping, we studied the valence band (VB) using XPS for $x$ = 0.0, 0.05, 0.1, and 0.35. Figure 6 demonstrates that the DOS near the Fermi level first significantly increases at $x$ = 0.05 and then drops at $x$ = 0.1 below the level of the undoped IONPs. The observed DOS increase at $x$ = 0.05 is consistent with the increase of a high spin fraction of the electronic system. This is also evident in the Fe 2p core and Fe 3p shallow core level evolution, while resulting in the increased $Fe^{2+}/Fe^{3+}$ ratio (Figure S7, Supporting Information). Liu et al.

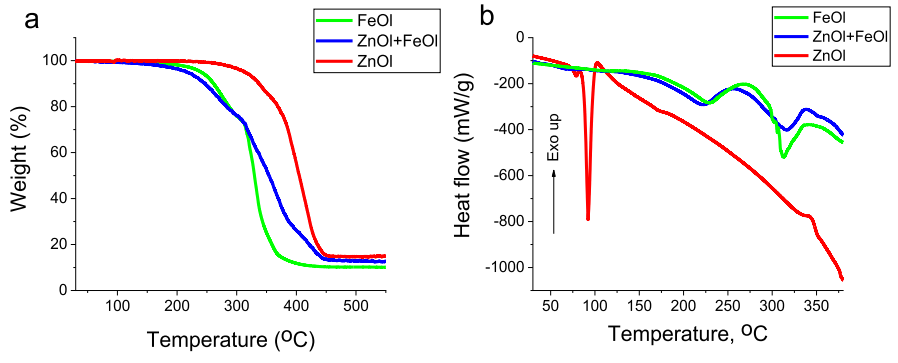


**Figure 5.** TGA (a) and DSC (b) curves of FeOl, ZnOl, and their mixture ($x$ = 0.35).



DOI: 10.1021/acsomega.8b02411
ACS Omega 2018, 3, 16328−16337

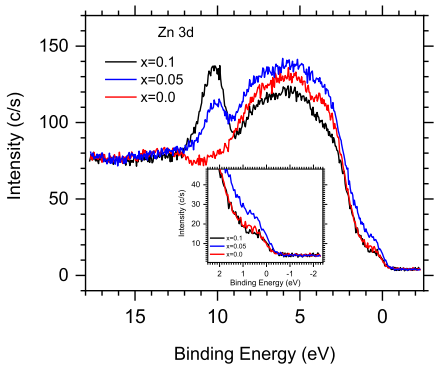


**Figure 6.** VB XPS spectra of $Zn_xFe_{3-x}O_4$ NPs at $x$ = 0.00, 0.05, and 0.1 at $h\nu$ = 1486.6 eV.

reported a similar behavior at very low doping level and attributed it to $Zn^{2+}$ ions initially occupying the A site.[53] However, when the A site is saturated, the $Zn^{2+}$ ions start occupying the high spin B site. A further increase of the doping level ($x$ = 0.35) does not significantly affect the density of the electron population at the Fermi level (Figure S8, Supporting Information), keeping it at the level of undoped IONPs. This observation is consistent with the photoemission data obtained for $Zn_xFe_{3-x}O_4$ films,[65] where the lowest doping level was $x$ = 0.5. A comparison of our data with standard iron oxides (Figure S9 and the text underneath, Supporting Information) shows similar DOS values.

These data demonstrate that for Zn-doped IONPs studied here, the normalized saturation magnetization values do not correlate with the initial DOS trend. For $x$ = 0.05, the DOS is the highest while the saturation magnetization is only slightly lower than that for undoped IONPs. For the high doping level ($x$ = 0.35), there is a correlation between the low magnetization and DOS, but for undoped IONPs, the DOS is as low as that for $x$ = 0.35, but the magnetization is the highest. To better understand such behavior, we further analyzed the Zn and Fe contents on the NP surface and subsurface. The Fe 2p/Zn 2p ratio is 28.4 for $x$ = 0.05, 5.5 for $x$ = 0.1, and then further decreases to 4 and 3 for $x$ = 0.19 and $x$ = 0.35, respectively. In subsurface layers, the Fe 3p/Zn 3p ratio changes from 99 to 37.5 to 13.5 and to 9.8 for $x$ = 0.05, 0.1, 0.19, and 0.35, respectively. These data indicate that the dependence upon doping is nonlinear and the most dramatic change in the surface and subsurface composition occurs between the samples obtained at $x$ = 0.05 and $x$ = 0.1, while at further doubling of Zn loading ($x$ = 0.19) the changes are less prominent.

Our observations indicate that the DOS is strongly influenced by the $Zn^{2+}$ ion distribution/accumulation on the IONP surface. When the $Zn^{2+}$ ion loading is low and the $Zn^{2+}$ ions are sparsely distributed in the IONP surface lattice, they substitute mainly $Fe^{3+}$ surface ions in the A sites[49] and do not interfere or rather enhance the charge carriers density at the B sites, resulting in the highest DOS near the Fermi level. This should correlate with an increase of the magnetization, but we do not observe such a correlation. If the initial occupation of the A site for $Zn^{2+}$ is preferred, then according to Neel's model,[66] diamagnetic $Zn^{2+}$ ions would not affect magnetization by merely their presence. Nevertheless, after doping, a decrease of the occupation fraction of $Fe^{3+}$ at the A site would reduce the magnetic moment of the A site and consequently increase the net magnetization. To explain the observed monotonic reduction of magnetization, an additional effect leading to a simultaneous decrease of the magnetic moment of the B site needs to be introduced. The spin canting in the B sublattice[67] could be a reason or an effect of antiphase boundaries (APB) reported for films;[68,69] however, APB free films have been reported as well.[41] Although the APB effect might be negligible for high quality thin films, it might significantly affect magnetic properties of NPs.

The further accumulation of $Zn^{2+}$ ions on the NP surface results in disrupting hopping mechanism between $Fe^{2+}/Fe^{3+}$ ions of the B sublattice, leading to the decreasing DOS. Thus, Zn doping allows tuning of the charge carrier density and influences both the conductivity and the saturation magnetization.

## CONCLUSIONS

We synthesized monodisperse Zn-doped IONPs of different compositions and studied their structure and properties. The IONP sizes were in the range of 16−25 nm depending on the reaction conditions, with IONP size distributions not exceeding 6%. Using XPS and EDS, we discovered a radial $Zn^{2+}$ ion distribution, with significant $Zn^{2+}$ ion enrichment on the IONP surface. Such species distribution was attributed to the different decomposition patterns of Zn and Fe oleates, as was shown by TGA and DSC. It was demonstrated that Zn oleate does not decompose at the reaction temperature (~340 °C), while the mixture of Zn and Fe oleates decomposes at even lower temperature than Fe oleate, revealing a mutual influence of $Zn^{2+}$ and forming IONPs on the decomposition process. The XPS data at the Fermi level demonstrated that at the low Zn loading, the moderate accumulation of $Zn^{2+}$ ions on the IONP surface increases the DOS, that is, the metallic character of these NPs with a largely preserved saturation magnetization, making them promising for spintronics applications.

## EXPERIMENTAL SECTION

**Materials.** Iron(III) chloride hexahydrate (Sigma-Aldrich, 97%), zinc chloride (Sigma-Aldrich, 98%), hexane (VWR analytical), sodium oleate (TCI, >97%), ethanol (Pharmco-Aaper, 200 proof), eicosane (Sigma-Aldrich, 99%), and docosane (Sigma-Aldrich, 99%) were used as received.

**Synthesis of Oleate Precursors.** FeOl was synthesized according to a published procedure.[29] For ZnOl synthesis, zinc chloride (2.17 g, 0.016 mol) and sodium oleate (9.67 g, 0.032 mol) were added to a mixture of ethanol (16 mL), hexane (28 mL), and water (37 mL) and left to react for 4 h at 70 °C under stirring. Upon cooling, a white powder formed which was separated by centrifugation and washed with 15 mL ethanol five times following centrifugation and supernatant removal each time. Subsequently, the product was dried under vacuum for 24 h at room temperature. Elemental analysis data (from X-ray fluorescence and combustion) (wt %) found: C, 68.95; O, 9.85; H, 10.56; Zn, 10.64. Calcd ($ZnC_{36}H_{66}O_4$): C, 68.97; O, 10.22; H, 10.53; Zn, 10.44.

**Synthesis of Undoped and Zn-Doped IONPs.** IONPs were prepared via the thermal decomposition of FeOl in eicosane or docosane.[32,48] In a typical experiment, a three-neck round-bottom flask furnished with a reflux condenser, a magnetic stir bar, and two septa was loaded with 1.66 g of FeOl, 1.69 mL of oleic acid (3 mmol), and 6.48 g of eicosane. One septum contained a temperature probe inserted in a glass



DOI: 10.1021/acsomega.8b02411
ACS Omega 2018, 3, 16328−16337

shield and through the other a long needle was inserted. The flask mounted in the heating mantel connected to a temperature controller was degassed three times using evacuation and filling with argon cycles and left under argon. The reaction mixture was then heated to 60 °C and kept at this temperature for 30 min to allow dissolution of the reagents in the melted solvent. After that the flask was heated with a heating rate of 2.2 °C/min to a boiling temperature (~340 °C) and was allowed to reflux for 30 min. The flask was cooled to 50 °C to keep the reaction solution liquid. The needed amount was precipitated by a mixture of hexane/acetone = 1:5 (v/v) and then washed once with the same mixture and twice with a hexane/acetone = 1:3 (v/v) mixture using centrifugation to separate the precipitate from supernatant. Finally, the precipitate was dispersed in chloroform. The NPs obtained were kept as solid reaction solutions until needed. Oxidation of as-synthesized NPs was performed following the procedure described elsewhere.[47,48] The reaction conditions for all the samples are summarized in Table 1. Because FeOl is a viscous oil, it was weighed first directly into the reaction flask, while the amounts of all other reagents were adjusted to keep the same ratio of metal oleates to oleic acid and the same concentration.

Zn-doped IONPs were synthesized similarly by adding required amounts of ZnOl (Table 1) to the reaction mixture. The rest of the procedure was the same as for IONP above.

**Characterization.** TEM was utilized for imaging of all samples. To prepare an electron-transparent NP sample, a drop of a chloroform solution was placed on a carbon-coated Cu grid. Images were obtained on a JEOL JEM 1010 transmission electron microscope at an accelerating voltage of 80 kV. HRTEM and STEM EDS images and maps were attained on a JEOL 3200FS transmission electron microscope with attached an Oxford Instruments INCA EDS system at an accelerating voltage of 300 kV.

XRD patterns were acquired using an Empyrean diffractometer (PANalytical). X-rays were produced from a copper target with a wavelength Cu K$\alpha$ of 1.54187 Å. Soller, antiscatter, and divergence slits as well as a nickel filter were in the beam path. The sample was spinning with a revolution time of 4 s during the measurement in reflection mode. The measurements were carried out with several step-sizes and counting rates.[70]

Elemental analysis of Fe and Zn oleates was carried out with an X-ray fluorescence spectrometer (Zeiss Jena VRA-30) furnished with a Mo anode, a LiF crystal analyzer, and an SZ detector. The Fe K$\alpha$ and Zn K$\alpha$ lines were used for analyses. Standards have been prepared by mixing 1 g of polystyrene with 10−20 mg of standard compounds.[71] The time of data acquisition was constant at 10 s. Carbon and hydrogen contents were determined by a combustion analysis.

The Zn and Fe contents in $Zn_{0.19}Fe_{2.81}O_4$ were measured using ICP−optical emission spectroscopy (NexION 300Q, PerkinElmer).

XPS experiments were carried out on the PHI VersaProbe II instrument equipped with a monochromatic Al K$\alpha$ source. The X-ray power of 25 W at 15 kV was utilized for a 200 $\mu$m beam size. The calibration of the instrument work function was performed to produce a BE of 84.0 eV for the Au $4f_{7/2}$ line for metallic gold and the spectrometer dispersion was tuned to produce BEs of 284.8 eV, 932.7 eV and of 368.3 eV for the C 1s line of adventitious (aliphatic) carbon present on the non-sputtered samples, Cu $2p_{3/2}$ and Ag $3d_{5/2}$ photoemission lines, respectively.[72] The PHI dual charge compensation system was utilized on all samples. The final VersaProbe II instrumental resolution was found to be better than 0.125 eV using the Fermi edge of the VB for metallic silver. XPS spectra with the energy step of 0.1 eV were recorded with SmartSoft-XPS v2.0 and processed using PHI MultiPack v9.0 software at pass energies of 46.95 and 23.5 eV for Fe 2p, 93.5 eV for Zn 2p, 23.5 eV for C 1s, VB and Fe 3p. Peaks were fitted utilizing a combination of Gaussians and Lorentzians with 10−50% of Lorentzian contents. Curve-fitting was carried out using a Shirley background. The samples for XPS measurements were prepared by drop casting of the NP solution onto the native surface of a Si(111) wafer.[73] The standards $Fe_2O_3$, $Fe_3O_4$, and FeO powders were commercially available from Sigma-Aldrich.

Thermal properties of the oleate precursors to Zn-doped IONPs were evaluated by TGA and DSC. TGA was performed on a Setaram Labsys evo STA 1600 instrument using alumina crucibles. DSC was analyzed on a TA Q200 analyzer with an RCS 90 cooling system using aluminum Tzero pans. All experiments were performed under an argon atmosphere while heating at 3 K/min.

The magnetic properties of the samples were acquired by a Superconducting Quantum Interference Device magnetometer (Quantum Design MPMS XL5). The measurements have been carried out using dried NPs on cotton placed in a gelatin capsule. The isothermal hysteresis loops, $M(H)$, were measured at fields $-1 \leq H \leq +1$ T. The dc magnetic susceptibility as a function of temperature, $M(T)$, was achieved down to 5 K using ZFC and FC protocols, at $H$ = 50 Oe.[21]

## ■ ASSOCIATED CONTENT

### Supporting Information

The Supporting Information is available free of charge on the ACS Publications website at DOI: 10.1021/acsomega.8b02411.

TEM image of the IONPs analogous to $Zn_{0.19}Fe_{2.81}O_4$; XRD patterns of the samples; HRTEM image of $Zn_{0.35}Fe_{2.65}O_4$; magnetization curves of IONPs; XPS spectra; and TEM image of the product of the Zn oleate decomposition (PDF)

## ■ AUTHOR INFORMATION


### Corresponding Authors

*E-mail: ylozovyy@indiana.edu (Y.L.).
*E-mail: lybronst@indiana.edu (L.M.B.).

### ORCID

Matthew N. Gordon: 0000-0001-7212-9047
Sara E. Skrabalak: 0000-0002-1873-100X
Lyudmila M. Bronstein: 0000-0002-0438-8132

### Present Address

#University of Illinois at Urbana−Champaign, Department of Chemistry, 505 South Mathews Av., Urbana, IL 61801.


### Author Contributions

The manuscript was written through contributions of all authors.

### Notes

The authors declare no competing financial interest.

## ■ ACKNOWLEDGMENTS

We thank the IU Nanoscale Characterization Facility for access to instrumentation as well as NSF grant #CHE-1048613 which



DOI: 10.1021/acsomega.8b02411
ACS Omega 2018, 3, 16328−16337

funded the Empyrean from PANalytical. IU Bloomington XPS facility was funded by NSF MRI grant (NSF DMR 1126394). The authors are especially thankful to Prof. Liang-shi Li for help with DSC measurements.

## REFERENCES

(1) Hellstern, D.; Schulze, K.; Schöpf, B.; Petri-Fink, A.; Steitz, B.; Kamau, S.; Hilbe, M.; Koch-Schneidemann, S.; Vaughan, L.; Hottiger, M.; Hofmann, M.; Hofmann, H.; von Rechenberg, B. Systemic distribution and elimination of plain and with Cy3.5 functionalized poly(vinyl alcohol) coated superparamagnetic maghemite nanoparticles after intraarticular injection in sheep in vivo. *J. Nanosci. Nanotechnol.* **2006**, *6*, 3261−3268.

(2) Briley-Saebo, K.; Bjørnerud, A.; Grant, D.; Ahlstrom, H.; Berg, T.; Kindberg, G. M. Hepatic cellular distribution and degradation of iron oxide nanoparticles following single intravenous injection in rats: implications for magnetic resonance imaging. *Cell Tissue Res.* **2004**, *316*, 315−323.

(3) Wang, Y. X. Superparamagnetic iron oxide based MRI contrast agents: Current status of clinical application. *Quant. Imag. Med. Surg.* **2011**, *1*, 35−40.

(4) Qu, Y.; Li, J.; Ren, J.; Leng, J.; Lin, C.; Shi, D. Enhanced Magnetic Fluid Hyperthermia by Micellar Magnetic Nanoclusters Composed of MnxZn1-xFe2O4 Nanoparticles for Induced Tumor Cell Apoptosis. *ACS Appl. Mater. Interfaces* **2014**, *6*, 16867−16879.

(5) Regmi, R.; Bhattarai, S. R.; Sudakar, C.; Wani, A. S.; Cunningham, R.; Vaishnava, P. P.; Naik, R.; Oupicky, D.; Lawes, G. Hyperthermia controlled rapid drug release from thermosensitive magnetic microgels. *J. Mater. Chem.* **2010**, *20*, 6158−6163.

(6) Bauer, L. M.; Situ, S. F.; Griswold, M. A.; Samia, A. C. S. High-performance iron oxide nanoparticles for magnetic particle imaging - guided hyperthermia (hMPI). *Nanoscale* **2016**, *8*, 12162−12169.

(7) Malyutin, A. G.; Easterday, R.; Lozovyy, Y.; Spilotros, A.; Cheng, H.; Sanchez-Felix, O. R.; Stein, B. D.; Morgan, D. G.; Svergun, D. I.; Dragnea, B.; Bronstein, L. M. Viruslike Nanoparticles with Maghemite Cores Allow for Enhanced MRI Contrast Agents. *Chem. Mater.* **2015**, *27*, 327−335.

(8) Zou, J.; Zhang, W.; Poe, D.; Qin, J.; Fornara, A.; Zhang, Y.; Ramadan, U. A.; Muhammed, M.; Pyykkö, I. MRI manifestation of novel superparamagnetic iron oxide nanoparticles in the rat inner ear. *Nanomedicine* **2010**, *5*, 739−754.

(9) Hemery, G.; Keyes, A. C.; Garaio, E.; Rodrigo, I.; Garcia, J. A.; Plazaola, F.; Garanger, E.; Sandre, O. Tuning Sizes, Morphologies, and Magnetic Properties of Monocore Versus Multicore Iron Oxide Nanoparticles through the Controlled Addition of Water in the Polyol Synthesis. *Inorg. Chem.* **2017**, *56*, 8232−8243.

(10) Kania, G.; Sternak, M.; Jasztal, A.; Chlopicki, S.; Błażejczyk, A.; Nasulewicz-Goldeman, A.; Wietrzyk, J.; Jasiński, K.; Skórka, T.; Zapotoczny, S.; Nowakowska, M. Uptake and bioreactivity of charged chitosan-coated superparamagnetic nanoparticles as promising contrast agents for magnetic resonance imaging. *Nanomedicine* **2018**, *14*, 131−140.

(11) Reguera, J.; Jiménez de Aberasturi, D.; Henriksen-Lacey, M.; Langer, J.; Espinosa, A.; Szczupak, B.; Wilhelm, C.; Liz-Marzán, L. M. Janus plasmonic-magnetic gold-iron oxide nanoparticles as contrast agents for multimodal imaging. *Nanoscale* **2017**, *9*, 9467−9480.

(12) Shen, Z.; Chen, T.; Ma, X.; Ren, W.; Zhou, Z.; Zhu, G.; Zhang, A.; Liu, Y.; Song, J.; Li, Z.; Ruan, H.; Fan, W.; Lin, L.; Munasinghe, J.; Chen, X.; Wu, A. Multifunctional Theranostic Nanoparticles Based on Exceedingly Small Magnetic Iron Oxide Nanoparticles for T1-Weighted Magnetic Resonance Imaging and Chemotherapy. *ACS Nano* **2017**, *11*, 10992−11004.

(13) Qiu, Y.; Tong, S.; Zhang, L.; Sakurai, Y.; Myers, D. R.; Hong, L.; Lam, W. A.; Bao, G. Magnetic forces enable controlled drug delivery by disrupting endothelial cell-cell junctions. *Nat. Commun.* **2017**, *8*, 15594.

(14) Salvatore, A.; Montis, C.; Berti, D.; Baglioni, P. Multifunctional Magnetoliposomes for Sequential Controlled Release. *ACS Nano* **2016**, *10*, 7749−7760.

(15) Shin, B. Y.; Cha, B. G.; Jeong, J. H.; Kim, J. Injectable Macroporous Ferrogel Microbeads with a High Structural Stability for Magnetically Actuated Drug Delivery. *ACS Appl. Mater. Interfaces* **2017**, *9*, 31372−31380.

(16) Tseng, Y.-J.; Chou, S.-W.; Shyue, J.-J.; Lin, S.-Y.; Hsiao, J.-K.; Chou, P.-T. A Versatile Theranostic Delivery Platform Integrating Magnetic Resonance Imaging/Computed Tomography, pH/cis-Diol Controlled Release, and Targeted Therapy. *ACS Nano* **2016**, *10*, 5809−5822.

(17) Ulbrich, K.; Holá, K.; Šubr, V.; Bakandritsos, A.; Tuček, J.; Zbořil, R. Targeted Drug Delivery with Polymers and Magnetic Nanoparticles: Covalent and Noncovalent Approaches, Release Control, and Clinical Studies. *Chem. Rev.* **2016**, *116*, 5338−5431.

(18) Zhu, K.; Deng, Z.; Liu, G.; Hu, J.; Liu, S. Photoregulated Cross-Linking of Superparamagnetic Iron Oxide Nanoparticle (SPION) Loaded Hybrid Nanovectors with Synergistic Drug Release and Magnetic Resonance (MR) Imaging Enhancement. *Macromolecules* **2017**, *50*, 1113−1125.

(19) Lee, N.; Yoo, D.; Ling, D.; Cho, M. H.; Hyeon, T.; Cheon, J. Iron Oxide Based Nanoparticles for Multimodal Imaging and Magnetoresponsive Therapy. *Chem. Rev.* **2015**, *115*, 10637−10689.

(20) Laurent, S.; Forge, D.; Port, M.; Roch, A.; Robic, C.; Vander Elst, L.; Muller, R. N. Magnetic Iron Oxide Nanoparticles: Synthesis, Stabilization, Vectorization, Physicochemical Characterizations, and Biological Applications. *Chem. Rev.* **2008**, *108*, 2064−2110.

(21) Kuchkina, N. V.; Morgan, D. G.; Kostopoulou, A.; Lappas, A.; Brintakis, K.; Boris, B. S.; Yuzik-Klimova, E. Y.; Stein, B. D.; Svergun, D. I.; Spilotros, A.; Sulman, M. G.; Nikoshvili, L. Z.; Sulman, E. M.; Shifrina, Z. B.; Bronstein, L. M. Hydrophobic Periphery Tails of Polyphenylenepyridyl Dendrons Control Nanoparticle Formation and Catalytic Properties. *Chem. Mater.* **2014**, *26*, 5654−5663.

(22) Yun, S.-H.; Sohn, B.-H.; Jung, J. C.; Zin, W.-C.; Lee, J.-K.; Song, O. Tunable Magnetic Arrangement of Iron Oxide Nanoparticles in Situ Synthesized on the Solid Substrate from Diblock Copolymer Micelles. *Langmuir* **2005**, *21*, 6548−6552.

(23) Kim, D.; Lee, N.; Park, M.; Kim, B. H.; An, K.; Hyeon, T. Synthesis of Uniform Ferrimagnetic Magnetite Nanocubes. *J. Am. Chem. Soc.* **2009**, *131*, 454−455.

(24) Kalidasan, V.; Liu, X. L.; Herng, T. S.; Yang, Y.; Ding, J. Bovine serum albumin-conjugated ferrimagnetic iron oxide nanoparticles to enhance the biocompatibility and magnetic hyperthermia performance. *Nano-Micro Lett.* **2016**, *8*, 80−93.

(25) Sun, S.; Zeng, H. Size-Controlled Synthesis of Magnetite Nanoparticles. *J. Am. Chem. Soc.* **2002**, *124*, 8204−8205.

(26) Li, Z.; Chen, H.; Bao, H.; Gao, M. One-Pot Reaction to Synthesize Water-Soluble Magnetite Nanocrystals. *Chem. Mater.* **2004**, *16*, 1391−1393.

(27) Redl, F. X.; Black, C. T.; Papaefthymiou, G. C.; Sandstrom, R. L.; Yin, M.; Zeng, H.; Murray, C. B.; O'Brien, S. P. Magnetic, Electronic, and Structural Characterization of Nonstoichiometric Iron Oxides at the Nanoscale. *J. Am. Chem. Soc.* **2004**, *126*, 14583−14599.

(28) Yu, W. W.; Falkner, J. C.; Yavuz, C. T.; Colvin, V. L. Synthesis of monodisperse iron oxide nanocrystals by thermal decomposition of iron carboxylate salts. *Chem. Commun.* **2004**, 2306−2307.

(29) Park, J.; An, K.; Hwang, Y.; Park, J.-G.; Noh, H.-J.; Kim, J.-Y.; Park, J.-H.; Hwang, N.-M.; Hyeon, T. Ultra-Large-Scale Syntheses of Monodisperse Nanocrystals. *Nat. Mater.* **2004**, *3*, 891−895.

(30) Kwon, S. G.; Piao, Y.; Park, J.; Angappane, S.; Jo, Y.; Hwang, N.-M.; Park, J.-G.; Hyeon, T. Kinetics of Monodisperse Iron Oxide Nanocrystal Formation by "Heating-Up" Process. *J. Am. Chem. Soc.* **2007**, *129*, 12571−12584.

(31) Jana, N. R.; Chen, Y.; Peng, X. Size- and Shape-Controlled Magnetic (Cr, Mn, Fe, Co, Ni) Oxide Nanocrystals via a Simple and General Approach. *Chem. Mater.* **2004**, *16*, 3931−3935.

(32) Bronstein, L. M.; Huang, X.; Retrum, J.; Schmucker, A.; Pink, M.; Stein, B. D.; Dragnea, B. Influence of Iron Oleate Complex



DOI: 10.1021/acsomega.8b02411
*ACS Omega* 2018, 3, 16328−16337

Structure on Iron Oxide Nanoparticle Formation. *Chem. Mater.* **2007**, *19*, 3624−3632.
(33) Zhao, Z.; Chi, X.; Yang, L.; Yang, R.; Ren, B. W.; Zhu, X.; Zhang, P.; Gao, J. Cation Exchange of Anisotropic-Shaped Magnetite Nanoparticles Generates High-Relaxivity Contrast Agents for Liver Tumor Imaging. *Chem. Mater.* **2016**, *28*, 3497−3506.
(34) Szczerba, W.; Żukrowski, J.; Przybylski, M.; Sikora, M.; Safonova, O.; Shmeliov, A.; Nicolosi, V.; Schneider, M.; Granath, T.; Oppmann, M.; Straßer, M.; Mandel, K. Pushing up the magnetisation values for iron oxide nanoparticles via zinc doping: X-ray studies on the particle's sub-nano structure of different synthesis routes. *Phys. Chem. Chem. Phys.* **2016**, *18*, 25221−25229.
(35) Wu, L.; Mendoza-Garcia, A.; Li, Q.; Sun, S. Organic Phase Syntheses of Magnetic Nanoparticles and Their Applications. *Chem. Rev. (Washington, DC, U.S.)* **2016**, *116*, 10473−10512.
(36) Mendoza-Garcia, A.; Sun, S. Recent Advances in the High-Temperature Chemical Synthesis of Magnetic Nanoparticles. *Adv. Funct. Mater.* **2016**, *26*, 3809−3817.
(37) Zhu, S.; Xu, X.; Rong, R.; Li, B.; Wang, X. Evaluation of zinc-doped magnetite nanoparticle toxicity in the liver and kidney of mice after sub-chronic intragastric administration. *Toxicol. Res.* **2016**, *5*, 97−106.
(38) Chen, F.; Bu, W.; Lu, C.; Chen, G.; Chen, M.; Shen, X.; Liu, R.; Shi, J. Hydrothermal Synthesis of a Highly Sensitive T2-Weigthed MRI Contrast Agent: Zinc-Doped Superparamagnetic Iron Oxide Nanocrystals. *J. Nanosci. Nanotechnol.* **2011**, *11*, 10438−10443.
(39) Maiti, D.; Saha, A.; Devi, P. S. Surface modified multifunctional ZnFe2O4 nanoparticles for hydrophobic and hydrophilic anti-cancer drug molecule loading. *Phys. Chem. Chem. Phys.* **2016**, *18*, 1439−1450.
(40) Daruka Prasad, B.; Nagabhushana, H.; Thyagarajan, K.; Nagabhushana, B. M.; Jnaneshwara, D. M.; Sharma, S. C.; Shivakumara, C.; Gopal, N. O.; Ke, S.-C.; Chakradhar, R. P. S. Temperature dependent magnetic ordering and electrical transport behavior of nano zinc ferrite from 20 to 800K. *J. Alloys Compd.* **2014**, *590*, 184−192.
(41) Venkateshvaran, D.; Althammer, M.; Nielsen, A.; Gepraegs, S.; Ramachandra Rao, M. S.; Goennenwein, S. T. B.; Opel, M.; Gross, R. Epitaxial ZnxFe3-xO4 thin films: A spintronic material with tunable electrical and magnetic properties. *Phys. Rev. B: Condens. Matter Mater. Phys.* **2009**, *79*, 134405.
(42) Hihath, S.; Kiehl, R. A.; Benthem, K. Interface composition between Fe3O4 nanoparticles and GaAs for spintronic applications. *J. Appl. Physiol.* **2014**, *116*, 084306.
(43) Sanz, M.; Oujja, M.; Rebollar, E.; Marco, J. F.; de la Figuera, J.; Monti, M.; Bollero, A.; Camarero, J.; Pedrosa, F. J.; García-Hernández, M.; Castillejo, M. Stoichiometric magnetite grown by infrared nanosecond pulsed laser deposition. *Appl. Surf. Sci.* **2013**, *282*, 642−651.
(44) Zhang, Y.; Liu, M.; Zhang, Y.; Chen, X.; Ren, W.; Ye, Z.-G. Atomic layer deposition of superparamagnetic and ferrimagnetic magnetite thin films. *J. Appl. Physiol.* **2015**, *117*, 17C743.
(45) Parkinson, G. S.; Diebold, U.; Tang, J.; Malkinski, L. *Tailoring the Interface Properties of Magnetite for Spintronics*; InTech, 2012; pp 61−88.
(46) Riaz, S.; Akbar, A.; Naseem, S. Structural, electrical and magnetic properties of iron oxide thin films. *Adv. Sci. Lett.* **2013**, *19*, 828−833.
(47) Gumina, G.; Easterday, R.; Malyutin, A. G.; Budgin, A. M.; Stein, B. D.; Nikoshvili, L. Z.; Matveeva, V. G.; Sulman, E. M.; Morgan, D. G.; Bronstein, L. M. γ-Fe2O3 nanoparticle surface controls PtFe nanoparticle growth and catalytic properties. *Nanoscale* **2013**, *5*, 2921−2927.
(48) Bronstein, L. M.; Atkinson, J. E.; Malyutin, A. G.; Kidwai, F.; Stein, B. D.; Morgan, D. G.; Perry, J. M.; Karty, J. A. Nanoparticles by Decomposition of Long Chain Iron Carboxylates: From Spheres to Stars and Cubes. *Langmuir* **2011**, *27*, 3044−3050.
(49) Harris, V. G.; Koon, N. C.; Williams, C. M.; Zhang, Q.; Abe, M.; Kirkland, J. P. Cation distribution in NiZn-ferrite films via extended x-ray absorption fine structure. *Appl. Phys. Lett.* **1996**, *68*, 2082−2084.
(50) Shtykova, E. V.; Huang, X.; Remmes, N.; Baxter, D.; Stein, B.; Dragnea, B.; Svergun, D. I.; Bronstein, L. M. Structure and Properties of Iron Oxide Nanoparticles Encapsulated by Phospholipids with Poly(ethylene glycol) Tails. *J. Phys. Chem. C* **2007**, *111*, 18078−18086.
(51) Huang, X.; Stein, B. D.; Cheng, H.; Malyutin, A.; Tsvetkova, I. B.; Baxter, D. V.; Remmes, N. B.; Verchot, J.; Kao, C.; Bronstein, L. M.; Dragnea, B. Magnetic Virus-like Nanoparticles in N. benthamiana Plants: A New Paradigm for Environmental and Agronomic Biotechnological Research. *ACS Nano* **2011**, *5*, 4037−4045.
(52) Jang, J.-t.; Nah, H.; Lee, J.-H.; Moon, S. H.; Kim, M. G.; Cheon, J. Critical enhancements of MRI contrast and hyperthermic effects by dopant-controlled magnetic nanoparticles. *Angew. Chem., Int. Ed.* **2009**, *48*, 1234−1238.
(53) Liu, X.; Liu, J.; Zhang, S.; Nan, Z.; Shi, Q. Structural, Magnetic, and Thermodynamic Evolutions of Zn-Doped Fe3O4 Nanoparticles Synthesized Using a One-Step Solvothermal Method. *J. Phys. Chem. C* **2016**, *120*, 1328−1341.
(54) Byrne, J. M.; Coker, V. S.; Cespedes, E.; Wincott, P. L.; Vaughan, D. J.; Pattrick, R. A. D.; van der Laan, G.; Arenholz, E.; Tuna, F.; Bencsik, M.; Lloyd, J. R.; Telling, N. D. Biosynthesis of Zinc Substituted Magnetite Nanoparticles with Enhanced Magnetic Properties. *Adv. Funct. Mater.* **2014**, *24*, 2518−2529.
(55) Mozaffari, M.; Shatooti, S.; Jafarzadeh, M.; Niyaifar, M.; Aftabi, A.; Mohammadpour, H.; Amiri, S. Synthesis of Zn2+ substituted maghemite nanoparticles and investigation of their structural and magnetic properties. *J. Magn. Magn. Mater.* **2015**, *382*, 366−375.
(56) Bera, S.; Prince, A. A. M.; Velmurugan, S.; Raghavan, P. S.; Gopalan, R.; Panneerselvam, G.; Narasimhan, S. V. Formation of Zinc Ferrite by Solid-state Reaction and its Characterization by XRD and XPS. *J. Mater. Sci.* **2001**, *36*, 5379−5384.
(57) Hawn, D. D.; DeKoven, B. M. Deconvolution as a Correction for Photoelectron Inelastic Energy Losses in the Core Level XPS Spectra of Iron Oxides. *Surf. Interface Anal.* **1987**, *10*, 63−74.
(58) Muhler, M.; Schoegl, R.; Ertl, G. The nature of the iron oxide-based catalyst for dehydrogenation of ethylbenzene to styrene 2. Surface chemistry of the active phase. *J. Catal.* **1992**, *138*, 413−444.
(59) Yamashita, T.; Hayes, P. Analysis of XPS Spectra of Fe2+ and Fe3+ Ions in Oxide Materials. *Appl. Surf. Sci.* **2008**, *254*, 2441−2449.
(60) Fujii, T.; de Groot, F. M. F.; Sawatzky, G. A.; Voogt, F. C.; Hibma, T.; Okada, K. In situXPS analysis of various iron oxide films grown byNO2-assisted molecular-beam epitaxy. *Phys. Rev. B: Condens. Matter Mater. Phys.* **1999**, *59*, 3195−3202.
(61) Somorjai, G. A. *Chemistry in Two Dimensions: Surfaces*; Cornell University Press: Ithaca, NY, 1981; p 41.
(62) Powell, C. J.; Jablonski, A. Evaluation of Calculated and Measured Electron Inelastic Mean Free Paths Near Solid Surfaces. *J. Phys. Chem. Ref. Data* **1999**, *28*, 19−62.
(63) Zhang, X.; Guo, G.; Ji, C.; Huang, K.; Zha, C.; Wang, Y.; Shen, L.; Gupta, A.; Bao, N. Efficient Thermolysis Route to Monodisperse Cu2ZnSnS4 Nanocrystals with Controlled Shape and Structure. *Sci. Rep.* **2014**, *4*, 5086.
(64) Baird, N.; Dittmar, J. W.; Losovyj, Y. B.; Pink, M.; Morgan, D. G.; Stein, B. D.; Torozova, A. S.; Krasnova, I. Y.; Grigoriev, M. E.; Sidorov, A. I.; Sulman, M. G.; Shifrina, Z. B.; Bronstein, L. M. Cr-containing magnetic oxides in a methanol synthesis: Does Cr ion distribution matter? *ChemistrySelect* **2017**, *2*, 6269−6276.
(65) Takaobushi, J.; Ishikawa, M.; Ueda, S.; Ikenaga, E.; Kim, J.-J.; Kobata, M.; Takeda, Y.; Saitoh, Y.; Yabashi, M.; Nishino, Y.; Miwa, D.; Tamasaku, K.; Ishikawa, T.; Satoh, I.; Tanaka, H.; Kobayashi, K.; Kawai, T. Electronic structures of Fe3-xMxO4 (M = Mn,Zn) spinel oxide thin films investigated by x-ray photoemission spectroscopy and x-ray magnetic circular dichroism. *Phys. Rev. B: Condens. Matter Mater. Phys.* **2007**, *76*, 205108.
(66) Neel, L. Proprietes Magnetiques des Ferrites-ferrimagnetism et Antiferromagnetisme. *Ann. Phys.* **1948**, *3*, 137−198.


DOI: 10.1021/acsomega.8b02411
*ACS Omega* 2018, 3, 16328−16337

(67) Yafet, Y.; Kittel, C. Antiferromagnetic arrangements in ferrites. *Phys. Rev.* **1952**, *87*, 290−294.
(68) Hibma, T.; Voogt, F. C.; Niesen, L.; van der Heijden, P. A. A.; de Jonge, W. J. M.; Donkers, J. J. T. M.; van der Zaag, P. J. Anti-phase domains and magnetism in epitaxial magnetite layers. *J. Appl. Phys.* **1999**, *85*, 5291−5293.
(69) Eerenstein, W.; Palstra, T. T. M.; Hibma, T.; Celotto, S. Origin of the increased resistivity in epitaxial Fe3O4 films. *Phys. Rev. B: Condens. Matter Mater. Phys.* **2002**, *66*, 201101.
(70) Patterson, S.; Arora, P.; Price, P.; Dittmar, J. W.; Das, V. K.; Pink, M.; Stein, B.; Morgan, D. G.; Losovyj, Y.; Koczkur, K. M.; Skrabalak, S. E.; Bronstein, L. M. Oriented Attachment Is a Major Control Mechanism To Form Nail-like Mn-Doped ZnO Nanocrystals. *Langmuir* **2017**, *33*, 14709−14717.
(71) Bronstein, L. M.; Ivanovskaya, A.; Mates, T.; Holten-Andersen, N.; Stucky, G. D. Bioinspired Gradient Materials via Blending of Polymer Electrolytes and Applying Electric Forces. *J. Phys. Chem. B* **2009**, *113*, 647−655.
(72) Jaquish, R.; Reilly, A. K.; Lawson, B. P.; Golikova, E.; Sulman, A. M.; Stein, B. D.; Lakina, N. V.; Tkachenko, O. P.; Sulman, E. M.; Matveeva, V. G.; Bronstein, L. M. Immobilized glucose oxidase on magnetic silica and alumina: Beyond magnetic separation. *Int. J. Biol. Macromol.* **2018**, *120*, 896−905.
(73) Baird, N.; Losovyj, Y.; Yuzik-Klimova, E. Y.; Kuchkina, N. V.; Shifrina, Z. B.; Pink, M.; Stein, B. D.; Morgan, D. G.; Wang, T.; Rubin, M. A.; Sidorov, A. I.; Sulman, E. M.; Bronstein, L. M. Zinc-containing Magnetic Oxides Stabilized by a Polymer: One Phase or Two? *ACS Appl. Mater. Interfaces* **2016**, *8*, 891−899.



DOI: 10.1021/acsomega.8b02411
*ACS Omega* 2018, 3, 16328−16337